

Revealing the structural evolution of CuAg composites during electrochemical carbon monoxide reduction

Received: 1 March 2024

Accepted: 23 May 2024

Published online: 01 June 2024

Di Wang^{1,6}, Hyun Dong Jung^{2,6}, Shikai Liu³, Jiayi Chen¹, Haozhou Yang¹, Qian He³✉, Shibo Xi⁴✉, Seoin Back²✉ & Lei Wang^{1,5}✉

Comprehending the catalyst structural evolution during the electrocatalytic process is crucial for establishing robust structure/performance correlations for future catalysts design. Herein, we interrogate the structural evolution of a promising Cu-Ag oxide catalyst precursor during electrochemical carbon monoxide reduction. By using extensive in situ and ex situ characterization techniques, we reveal that the homogenous oxide precursors undergo a transformation to a bimetallic composite consisting of small Ag nanoparticles enveloped by thin layers of amorphous Cu. We believe that the amorphous Cu layer with undercoordinated nature is responsible for the enhanced catalytic performance of the current catalyst composite. By tuning the Cu/Ag ratio in the oxide precursor, we find that increasing the Ag concentration greatly promotes liquid products formation while suppressing the byproduct hydrogen. CO₂/CO co-feeding electrolysis and isotopic labelling experiments suggest that high CO concentrations in the feed favor the formation of multi-carbon products. Overall, we anticipate the insights obtained for Cu-Ag bimetallic systems for CO electroreduction in this study may guide future catalyst design with improved performance.

Electrochemical CO₂ reduction (CO₂R) coupled with renewable electricity has been recognized as a promising route for mitigating the pressing carbon emission and enabling the sustainable production of value-added chemicals^{1–8}. Mechanistically, CO is the key reaction intermediate for the conversion of CO₂ to valuable multi-carbon (C₂₊) products during CO₂R⁹. Thus, great efforts have been made to the investigation of electrochemical CO reduction (COR) aiming to uncover the levers (i.e., catalyst structure, composition, micro-environment) that control the selectivity and activity towards C₂₊ products^{10–18}. On the other hand, tremendous success has been achieved for the development of efficient catalysts for CO₂R to CO^{19–26},

offering opportunities for converting CO₂ to C₂₊ products via a cascade approach (CO₂ → CO → C₂₊). Additionally, direct COR can effectively mitigate the severe issues associated with carbonate formation during CO₂R and lead to improved carbon utilization efficiency and system stability of the process. Therefore, there is a need to continue develop COR with the goal of achieving maximized activity and selectivity toward the desired products.

To date, Cu-based materials are the only known catalysts that exhibit appreciable activity and Faradaic Efficiencies (FE) in producing C₂₊ products during COR^{27,28}. Despite their potential, the unsatisfactory performance of Cu catalysts under practical relevant conditions

¹Department of Chemical and Biomolecular Engineering, College of Design and Engineering, National University of Singapore, Singapore, Singapore.

²Department of Chemical and Biomolecular Engineering, Institute of Emergent Materials, Sogang University, Seoul, Republic of Korea. ³Department of Materials Science and Engineering, College of Design and Engineering, National University of Singapore, Singapore, Singapore. ⁴Institute of Sustainability for Chemicals, Energy and Environment (ISCE2), Agency for Science, Technology and Research (A*STAR), Singapore, Singapore. ⁵Centre for Hydrogen Innovations, National University of Singapore, Singapore, Singapore. ⁶These authors contributed equally: Di Wang, Hyun Dong Jung.

✉ e-mail: heqian@nus.edu.sg; xi_shibo@isce2.a-star.edu.sg; sback@sogang.ac.kr; wanglei8@nus.edu.sg

has hindered the practical implementation of this technology. A handful of strategies have been explored to modify the physico-chemical properties of Cu catalysts, such as controlling the particle size, morphology, facet, grain boundaries and compositions, intending to develop catalysts with improved activity and selectivity for COR. Increasingly, bimetallic materials formed by introducing a second metal to Cu are being explored as a promising approach to tune the activity and selectivity of Cu catalysts for COR. For instance, bimetallic catalysts such as CuAu²⁹, CuPd^{30,31} and CuAg^{32–35} have been investigated for their potential for efficient COR. Particularly, CuAg-based materials have received significant attentions owing to their promising performance towards COR and CO₂R^{36–42}. In these researches, phase separation and alloy represent two forms of CuAg materials. In phase-separated CuAg materials, there is a clear interface between Cu/Ag, which is considered as active sites of the reaction^{32,42}. In CuAg alloy, a small amount of Ag is doped into the Cu lattice, and the Cu atoms around Ag are claimed to promote the production of C₂₊³⁷.

During the preparation of our manuscript, a few Ag-modified oxide-derived Cu catalysts were recently reported elsewhere showing improved FEs toward C₂₊ liquid products in COR^{32–34}. We also prepared Cu/Ag mixed-oxide precursors and employed them for COR, as the Cu and Ag atoms are initially well mixed within the precursors. The catalysts in our work are labeled based on the atomic ratios of Cu and Ag employed during preparation. For instance, Cu₃Ag₇ represents an atomic ratio of 3:7 between Cu and Ag. Besides, a-Cu₃Ag₇ denotes the as-prepared Cu₃Ag₇ precursor. Inductively Coupled Plasma Optical Emission spectroscopy (ICP-OES) indicate consistent Cu to Ag ratios in post-COR samples compared to the corresponding as-prepared samples (Supplementary Table 1). As shown in Fig. 1a, the CuAg catalysts used in our study and the previous work exhibit nearly identical selectivity at similar COR current densities, i.e., high FEs of >90% towards C₂₊ products were achieved with 60% of which being liquid products including ethanol, acetate and propanol³⁴. Additionally, the catalysts were found to both have uniform distributions of Cu and Ag within oxide precursors, as shown in the X-ray Energy Dispersive Spectroscopy (XEDS) elemental map (Fig. 1b). Notably, no obvious segregations of Ag or Cu were observed for both catalysts even after extended period of COR reactions (Supplementary Figs. 4 and 5). At first glance, this may lead to the conclusion of that the active phase of this bimetallic catalyst is the solid solution of Cu and Ag. However, it is contradictory to the immiscibility nature of Cu and Ag (Fig. 1c), i.e., the solubility of Cu in Ag or vice versa are largely illegible at temperatures below 300 °C⁴³. Therefore, we hypothesize that the Cu and Ag co-exist in other forms post COR, such as core-shell type of structures, induced by significant structural evolutions of the Cu/Ag oxide precursors during COR. Additionally, CuAg catalysts with higher Ag contents

exhibited increased selectivity towards C₂₊ products, suggesting that the COR selectivity is closely related to the structure formed by CuAg with different Cu/Ag ratio. Overall, the above surprising observations have motivated us to carefully explore the detailed structural evolution of the Cu/Ag oxide precursors during COR, and determine the true active phase that are responsible for the high selectivity and activity towards C₂₊ products.

In this work, comprehensive physical characterizations, including scanning transmission electron microscopy (STEM), *operando* X-ray absorption fine structure spectroscopy (XAFS), X-ray diffraction analysis (XRD) and X-ray photoelectron spectroscopy (XPS) were employed to track the dynamic structural evolution of Cu/Ag oxides during COR. Our findings suggest that Cu/Ag oxide precursors transformed to phase-separated Cu and Ag metallic states during COR under practical relevant conditions. Taking the Cu/Ag oxide with optimized composition (Cu₃Ag₇) as an example, both the Cu and Ag oxides were reduced into metallic forms during COR. The bimetallic material underwent structural transformation and formed small Ag particles wrapped with thin and amorphous Cu layers. Our computational investigations based on Density Functional Theory (DFT) indicate that the amorphous Cu on top of Ag lattice exhibits stronger bindings towards CO* and CH₃CHO*, which lead to the favorable formation of C₂₊ products, i.e., ethanol. Furthermore, through CO₂/CO co-feeding electrolysis together with isotopic labeling, we identified that most of C₂₊ products were derived from CO rather than CO₂, consistent with recent findings reported elsewhere⁴⁴. Specifically, the introduction of CO gas feeds resulted in an increased formation of C₂₊ products, indicating that under our experimental conditions, COR exhibits higher activity for C₂₊ products formation of compared to CO₂R. This highlights the advantages of conducting COR. Notably, in CuAg samples, this phenomenon is further enhanced with the addition of Ag. Overall, our study reveals that the Ag-induced amorphous Cu is the origin of the improved selectivity and activity towards C₂₊ products, particularly liquid products. These insights will contribute to our understanding of the mechanism of COR and the design strategies for catalysts.

Results

Physical characterizations of Cu/Ag oxides before and after COR

The typical Cu/Ag oxide precursors and the pristine CuO control samples were prepared according to a modified co-precipitation approach³⁴. As depicted by the Scanning Electron Microscope (SEM) images (Fig. 2a and Supplementary Figs. 1 and 2), the as-prepared CuO exhibit flaky morphology. Upon the introduction of Ag, rod-shaped particles with diameters ranging from 500 nm to 2 μm become dominant in the CuAg oxides. After conducting the COR measurement, no

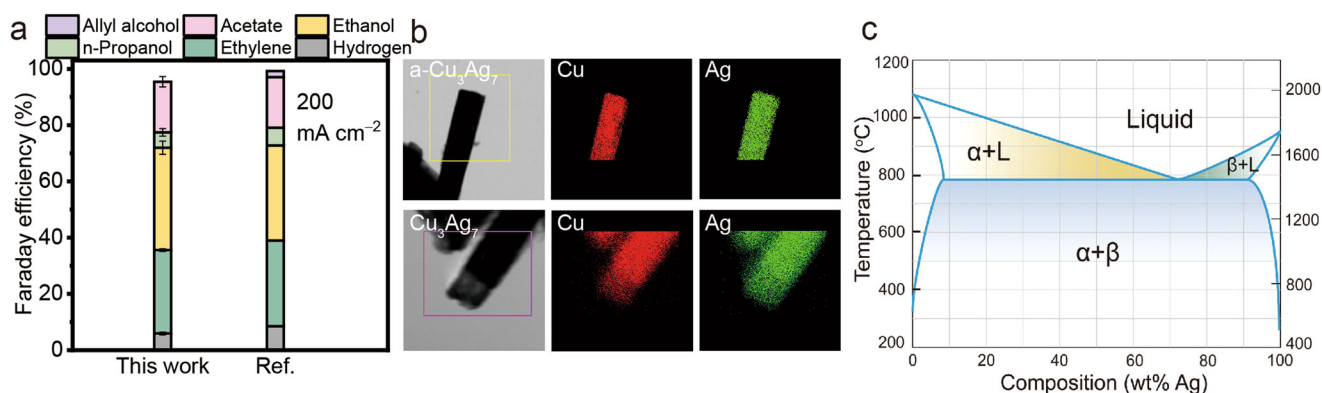


Fig. 1 | COR performance on CuAg and structural information of Cu and Ag. **a** Faradaic efficiency (FE) of the CuAg samples in this work and reference work³⁴. **b** XEDS elemental mapping of as-prepared Cu/Ag precursors and post-reacted

CuAg catalysts. **c** Phase diagram of CuAg. The error bars represent standard deviations from at least three independent measurements. Relevant source data are provided as a Source Data file.

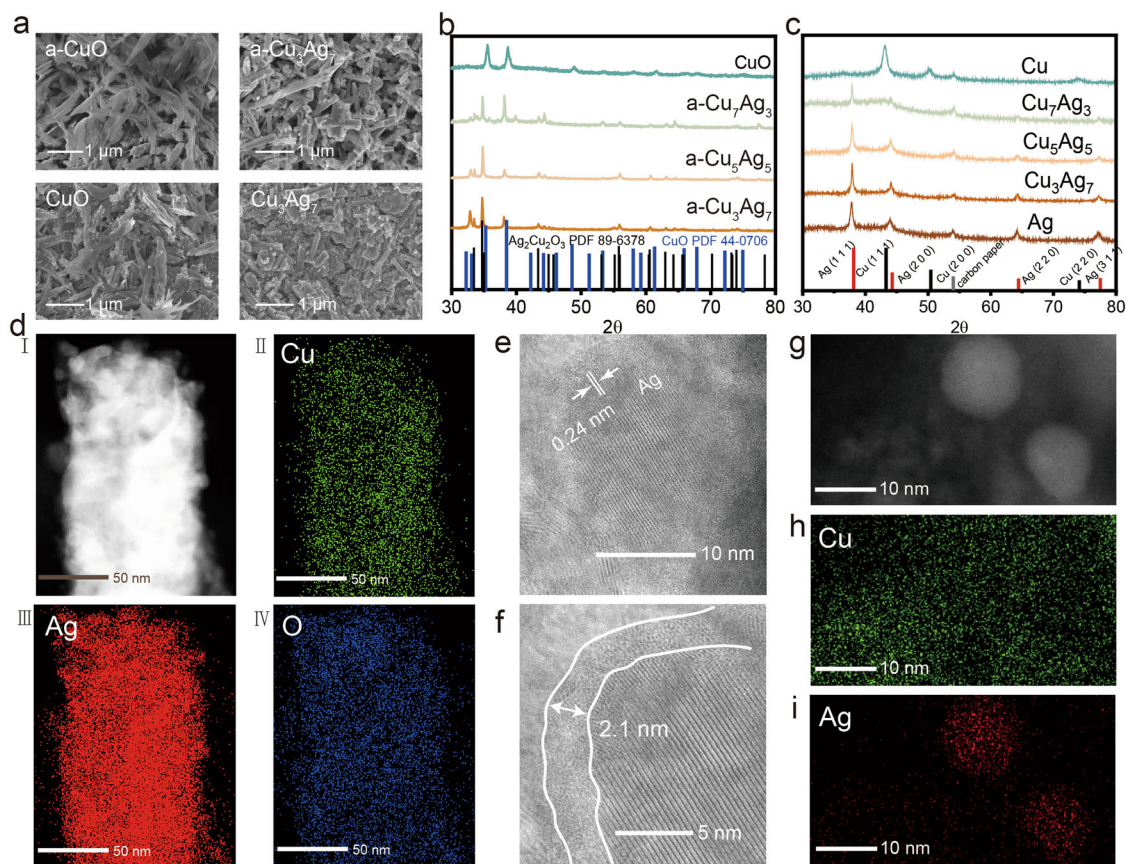


Fig. 2 | Structural characterization of CuO and Cu₃Ag₇ catalysts before and after COR at 200 mA cm⁻². **a** SEM images of as-prepared CuO (a-CuO) and Cu₃Ag₇ (a-Cu₃Ag₇) precursors and post-COR CuO and Cu₃Ag₇ samples. **b** XRD patterns of as-prepared CuO and CuAg precursors. **c** XRD patterns of post-reacted CuO and CuAg catalysts. **d** STEM XEDS elemental mapping of post-reacted Cu₃Ag₇ catalyst.

e, f HRTEM images of rod-shaped particles edge in post-reacted Cu₃Ag₇. **g** STEM image of nanoparticles on the surface of post-reacted Cu₃Ag₇. **h, i** STEM XEDS elemental mapping of nanoparticles on the surface of post-reacted Cu₃Ag₇. Relevant source data are provided as a Source Data file.

significant morphological changes were observed in any of these samples. However, small particles with diameters of approximately 10 nm were discovered to have accumulated on the surface of these samples. This phenomenon could be attributed to the dissolution of Cu and/or Ag in the electrolyte under open circuit voltage (OCV), followed by their redeposition back to the catalyst surface^{45,46}. XRD was employed to investigate the crystallographic structures of catalysts before and post COR. Figure 2b demonstrates the composition of the as-prepared precursors, which comprised CuO and Ag₂Cu₂O₃. Notably, Ag₂Cu₂O₃ is a singular Cu/Ag compound, characterized by a uniform distribution of Cu and Ag, as shown in Fig. 1b, however, with distinct oxidation states^{47–49}. This is consistent with our observation in Fig. 1b. However, out of our expectation, the XRD spectra of the post-COR Cu/Ag samples only show the patterns of metallic Ag (Fig. 2c), while no Cu-related peaks were detected. Hence, drastic structural evolution must have taken place in these CuAg oxide samples during COR. To interpret this phenomenon, we have contemplated three potential scenarios. Firstly, we speculate that Cu may be largely dissolved in the KOH electrolyte during the COR electrolysis. However, XEDS analysis in Fig. 2d reveals that Cu could be easily detected in the post-COR sample, indicating that majority of the Cu content retained during COR. This has been corroborated by the subsequent XPS data (vide infra). Second, Cu existed in the post-COR sample in the form of extremely small clusters, which led to a significant reduction of its X-ray diffraction peak intensity. However, the persistence of small Cu clusters without aggregation during COR appears unlikely due to the low cohesive energy of Cu. Besides, there were no evidences found to

substantiate this assumption. Lastly, we hypothesize that the CuO within the Cu/Ag precursor was reduced to metallic Cu and underwent a structural transformation into an amorphous state under the conditions of COR^{50–52}. The XRD of Cu₃Ag₇ samples after a short period of COR under 200 mA cm⁻² was also conducted (Supplementary Fig. 12b). Within 10 min of COR, all Cu-related peaks disappeared, indicating the rapid formation of amorphous Cu.

To verify this hypothesis, we conducted post-COR STEM to carefully examine the morphological structure and composition of the CuAg samples. Taking Cu₃Ag₇ as an example, its mesostructured and elemental composition retained after COR (Fig. 2d). The utilization of high-resolution STEM with atomic sensitivity enabled us to observe the sample's composition with exceptional clarity. As shown in Fig. 2e, small Ag nanoparticles exist in the post-COR sample, exhibiting an interplanar spacing of approximately 0.24 nm, corresponding to the Ag (111) crystal plane⁵³. Remarkably, the Ag particles were found to be enveloped in an amorphous layer with an average thickness of ~2 nm (Fig. 2f). The composition of this layer was further confirmed to be Cu by the corresponding XEDS elemental mapping (Supplementary Fig. 6), which agrees well with the above XRD analysis. Drawing upon previous research, this amorphous Cu layer can be attributed to in situ self-reconstruction induced electroactive amorphous species (ISIA)^{54–60}. Such layers can emerge during electrocatalysis as a consequence of factors like potential driving, lattice distortion, and defect induction, etc. The formation of ISIA often correlated with changes in electrocatalytic activity that deserves further study^{61,62}. For instance, crystalline In₂O₃ was reconstructed to

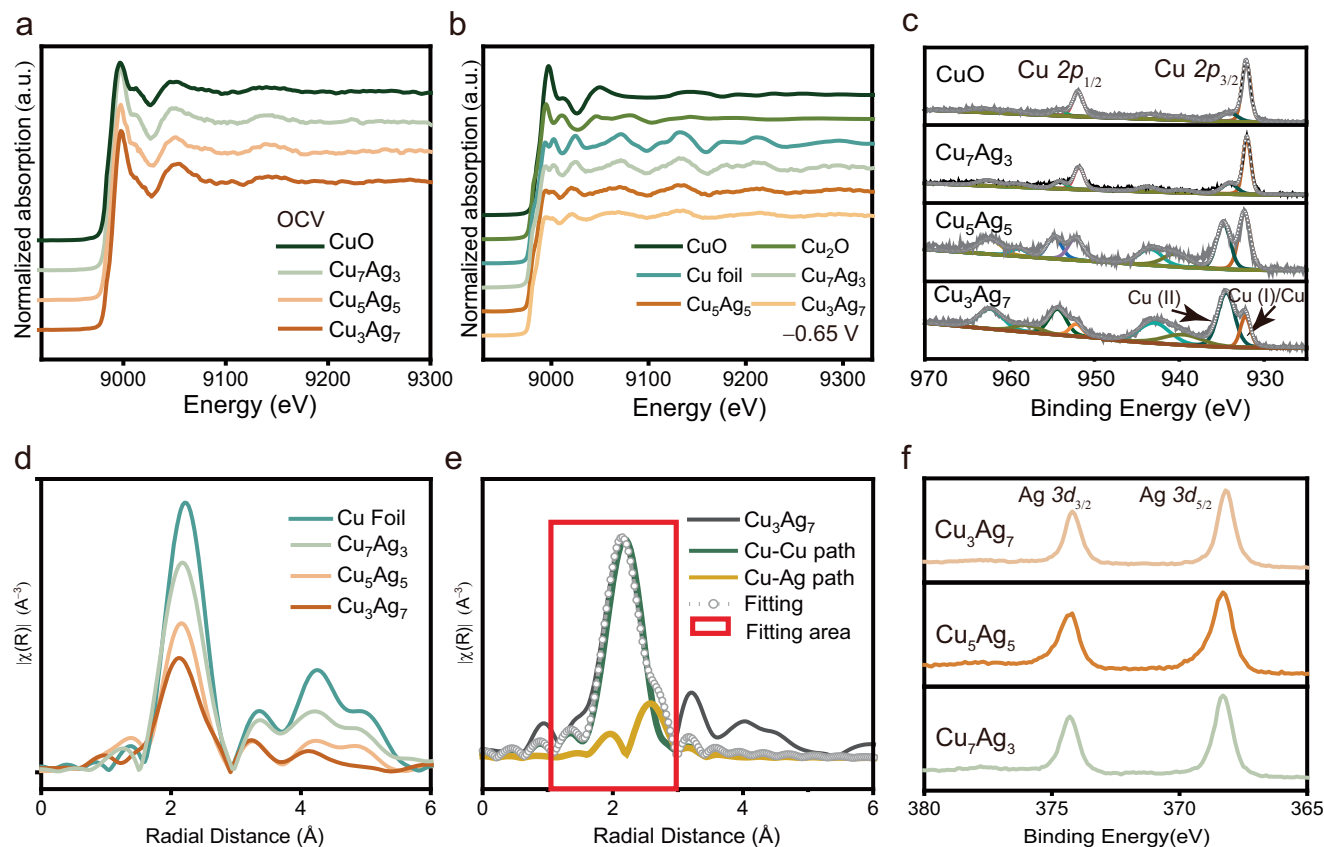


Fig. 3 | XPS and Operando XAFS spectra of CuO and CuAg samples. a Cu K-edge XANES and EXAFS spectra of the CuO and CuAg samples at OCV. **b** Cu K-edge XANES and EXAFS spectra of CuAg samples at -0.65 V vs RHE (~ 150 mA cm^{-2}), Cu_2O , CuO and standard Cu foil. **d** FT of EXAFS spectra of CuAg samples at -0.65 V

vs RHE and standard Cu foil. **e** EXAFS fitting curves at the Cu–Cu path and Cu–Ag path for Cu_3Ag_7 at -0.65 V vs RHE. **c**, **f** XPS spectra of CuO and CuAg samples after COR with 200 mA cm^{-2} of **(c)** Cu $2p$ and **(f)** Ag $3d$. Relevant source data are provided as a Source Data file.

crystalline In and amorphous $\text{In}_2\text{O}_{3-x}$ during CO_2R , showing enhanced FE ($\sim 90\%$) towards formate⁵⁶. Moreover, chlorine doping induced the formation of amorphous $\text{LiCoO}_{1.8}\text{Cl}_{0.2}$, showcasing enhanced activity and stability in oxygen evolution reaction (OER)⁵⁷. Previously, it has been reported that Cu atoms show higher mobility in CuAg materials under CO_2R conditions, potentially leading to their migration toward the electrode surface^{42,63}. Since atomic transfer mechanism is considered as a major contributor to the formation of ISIA, we hypothesize that Cu atoms will migrate to CuAg surface under COR condition. For instance, the reduction of oxidized Cu, and the redeposition of the dissolved Cu in alkaline electrolyte, i.e., KOH used in this work. Besides, since Cu and Ag are difficult to form a uniform alloy under normal conditions⁶⁴, the high Ag content in the CuAg samples likely induce lattice mismatches and results in a spatial strain effect between Cu and Ag⁶⁵, which disrupt the formation of crystalline Cu, and causing amorphization of surface Cu. Taken together, we believe the combined effects of cathodic potential during COR, redeposition process of Cu and lattice mismatch induced by Ag lead to the formation of amorphous Cu layers around the Ag particles.

In addition, the STEM images (Fig. 2f) clearly show the interface between Cu and Ag, indicating that Cu and Ag are phase segregated. Such arrangement of Cu and Ag is consistent with the apparent “uniform distributions” of Cu and Ag elements as suggested by the XEDS elemental mappings in this study (Fig. 2g–i) and in previous work^{34,66}. In all, we believe that the homogenous Cu/Ag oxide precursors undergo a transformation to a bimetallic composite consisting of small Ag nanoparticles enveloped by thin layers of amorphous Cu under the COR conditions.

Tracking the dynamic structural evolution of CuAg during COR

Operando measurements based on XAFS were employed to further explore the structural evolution of the CuAg catalyst during COR. To ensure the relevance of the operando XAFS experiments, identical flow cell (Supplementary Fig. 8) and COR conditions (i.e., CO feeding rate, electrolyte, electrode potential, etc.) were employed for the XAFS experiments. In a typical experiment, both the X-ray absorption near-edge structure (XANES) and extended X-ray absorption fine structure (EXAFS) of Cu K-edge were measured for the pristine CuO and various CuAg samples at Open Circuit Voltage (OCV) and -0.65 V vs. RHE, respectively. As shown in Fig. 3a, the Cu-XANES spectra suggest that the chemical states of Cu in these samples are in +2 oxidation state (CuO) under the OCV condition^{67–69}, consistent with the above XRD and XPS results. When a negative potential was applied to drive COR, the Cu K-edge absorption edge positions for all samples decreased from 8976 to 8974 eV (Fig. 3b), indicating the valence state of Cu decreased during COR. Since the Cu absorption edge positions of all CuAg samples are nearly identical to that of the standard Cu foil, we believe that the valence state Cu was reduced to its metallic state for all CuAg samples under COR conditions. Rather than valence state, EXAFS fingerprints provide coordination information of the CuAg samples during COR^{70,71}. As shown in Fig. 3b, the two peaks located at around 9000 eV in the CuAg samples exhibited notable differences compared to the spectrum of standard Cu foil. Specifically, as the Ag concentration increased, the peak at 9002 eV became flatter, and the peak at 9025 eV shifted towards lower binding energies. To closely examine the atomic structure of CuAg, the Fourier transform (FT) of EXAFS under reaction conditions is analyzed. As shown in Fig. 3d, in the R space, the intensity of the peak at ~ 2.4 Å decreases with the increasing

Ag content, indicating a reduction in the coordination number of Cu within the CuAg samples⁷². In addition, we conducted curve fitting for the FT-EXAFS spectra of Cu₃Ag₇ to extract detailed information regarding the neighboring atomic species, coordination number and distance (Fig. 3e). The fitting results revealed that in Cu₃Ag₇, the average coordination number of Cu is ~7.6, comprising 6.1 Cu–Cu bonds and 1.5 CuAg bonds (Supplementary Table 6). The total coordination number, which is lower than the typical 12 found in fcc metals like Cu foil for comparative analysis, may stem from the amorphous characteristic of the Cu layer and the immiscibility nature of Cu and Ag. Furthermore, the FT-EXAFS results of CuAg samples in Fig. 3d also demonstrate that with the addition of Ag, the structure of Cu in CuAg undergoes significant evolution. Specifically, the intensity of the peak located at around 4.3 Å decreases significantly with the increase in Ag content within the CuAg samples, indicating a reduction in long-range order of Cu atom arrangement^{73,74}. Combining observations from both STEM and XRD analyses, we believe that this reduction in long-range order of Cu can be attributed to both the incorporation of Ag foreign atoms, as well as the formation of amorphous Cu layer. This is supported by the substantially decreased coordination number of Cu in Cu₃Ag₇ (Supplementary Table 6). Notably, amorphous Cu was observed solely in CuAg samples with high Ag contents (Fig. 2e, f). Besides, there are no XRD patterns related to crystalline Cu observed in the post-COR CuAg samples (Fig. 2c), while pristine CuO sample did not exhibit such behavior. Hence, we hypothesize that the large Ag content exist in CuAg samples likely plays a role in the formation of amorphous Cu during COR.

XPS was also employed to determine the surface composition of the samples before and after COR. As anticipated, both Ag and Cu in the precursors predominantly exist in their respective oxidation states prior to COR (Supplementary Fig. 13). The labeled Cu 2p_{3/2} peak in Fig. 3c is corresponding to Cu (I)/Cu for post-reacted CuO and CuAg samples (Supplementary Fig. 14). Thus, after COR, the bulk CuO catalyst predominantly exhibits the form of metallic Cu and Cu (I) (Fig. 3c). The presence of Cu (I) and Cu (II) species can be attributed to the native oxide layers formed during the XPS sample preparation. Notably, upon the introduction of Ag, the post-COR CuAg samples show an increased portion of the Cu (II) species, and this increase scales with Ag content within the bimetallic materials (Fig. 3c). Considering that each sample was subjected to identical post-reaction treatments for XPS, this observation is likely attributable to the presence of the thin layer of amorphous Cu within the CuAg samples. This thin layer renders the Cu more prone to oxidation upon exposure to air. In the contrary, as shown in Fig. 3f, Ag within all CuAg samples was reduced to the metallic state. Furthermore, there was no discernible peak position shift for Ag across different samples, indicating a consistent Ag state across the various CuAg samples. Nevertheless, we believe the presence of Ag substantially influences the structural evolution of Cu in CuAg materials, i.e., Cu transition to an amorphous state during COR, especially with higher Ag content.

The dynamic structural evolution of the catalyst during COR/CO₂R will result changes in product selectivity^{75–77}, thus, the structural evolutions of various CuAg catalyst precursors with different Cu/Ag ratios were investigated through XRD, STEM, and *operando* XAFS (Supplementary Fig. 12). Specifically, COR tests with reaction time ranging from 10 min to 10 h were performed in combination with the above physical characterizations. As shown in Supplementary Fig. 12b, XRD results indicate the absence of patterns corresponding to crystalline Cu from the initial 10 minutes of the reaction, a trend that persists consistently over the course of 10 hours. This indicates a rapid formation of the amorphous Cu layer under COR conditions, and the amorphous Cu layer remains relatively stable over an extended duration. Through ex situ STEM analysis, we further confirm the presence of an outer layer of amorphous Cu on top of the crystalline Ag nanoparticles. As depicted in Supplementary Fig. 12a, following COR for the

durations of 1, 5, and 10 h, Cu amorphous layers with an approximate width of 2–3 nm are always observed at the periphery of rod-shaped particles, consistent with the phenomenon observed in XRD. However, due to the immiscibility of Cu and Ag, we hypothesize that the phase separation between Cu and Ag will become more pronounced with longer reaction times, potentially weakening the influence of Ag on the structural evolution of Cu. Hence, we do not exclude the possibility of crystalline Cu particle formation after prolonged COR (*vide infra*). Moreover, the *operando* XAFS collected at different COR durations clearly demonstrate the reduction of the long-range ordered structure of Cu with the increase of Ag content. As shown in Supplementary Fig. 12d, after COR on Cu₃Ag₇ samples for 1, 5, and 10 h, the structural integrity of Cu in Cu₃Ag₇ is essentially maintained, and the long-range order of Cu after 5 and 10 h of COR remains substantially lower than that of the Cu foil, suggesting that the low Cu crystallinity can be maintained under COR conditions for prolonged reaction times. Finally, COR products were also collected and quantified to demonstrate the robust COR activity and selectivity during these COR assessments (Supplementary Fig. 12e).

Catalyst structure/performance correlations

The electrochemical COR performance of CuAg and CuO were assessed using a gas diffusion electrode-based flow cell with 1.0 M KOH as the electrolyte. The gaseous and liquid products were detected and quantified by gas chromatography (GC) and Nuclear Magnetic Resonance (NMR) spectroscopy, respectively. We first conducted COR on a pristine Ag catalyst under the identical conditions (Supplementary Fig. 15), where H₂ was observed as the only product, suggesting that Ag is inert in further reducing CO, at least under our testing conditions. Figure 4a presents the product distributions of COR on CuO and on CuAg with various Cu/Ag ratio at 200 mA cm⁻². First, the CuAg bimetallic materials demonstrate slightly improved selectivity towards C₂₊ products in comparison to the pristine CuO sample. This improvement is predominantly due to the suppressed H₂ production, notably pronounced for the CuAg catalyst with high Ag content (Supplementary Fig. 16). As shown in Fig. 4a, despite the marginal enhancement on the C₂₊ selectivity, the CuAg catalysts, i.e., Cu₅Ag₅ and Cu₃Ag₇, exhibit substantially reduced overpotentials (~0.1 V) at 200 mA cm⁻² compared to those of the pristine CuO. Given their comparable electrochemical active surface areas (ECSA, Supplementary Fig. 17), we believe that these CuAg bimetallic catalysts show enhanced intrinsic activity towards CO reduction. Specifically, the Cu₃Ag₇ exhibits the highest selectivity towards C₂₊ products, with over 60% being liquid products, i.e., ethanol, acetate, and small portions of propanol. However, when the Ag content further increases (Cu₁Ag₉), the generation of methane becomes notable on the expense of C₂₊ selectivity. This is possibly due to the insufficient Cu-active sites, leading to the increased COR concentration overpotential (Fig. 4a). We further compared the partial current densities of each C₂₊ products on these CuAg catalysts. The results, depicted in Fig. 4b, reveal that with an increase in the Ag content, the production distribution shifts from gaseous product (ethylene) to liquid products (mainly ethanol and acetate). Worth noting, the formation of n-propanol also decreases along with ethylene upon the addition of Ag, possibly indicating a potential shared pathway and/or intermediates between these two products. Similar hypothesis was made elsewhere recently⁷⁸. Furthermore, taking Cu₃Ag₇ as an example, its high selectivity towards C₂₊ products is sustained even under higher current densities (Fig. 4d), with only negligible increase in the H₂ selectivity, showing its promise for future implementations. Overall, the selectivity towards liquid products is enhanced in the CuAg samples (Fig. 4c), along with an improvement in combined C₂₊ products primarily due to the suppressed H₂ production.

As discussed above, the substantial Ag content with the bimetallic materials fosters the formation of amorphous Cu layers characterized

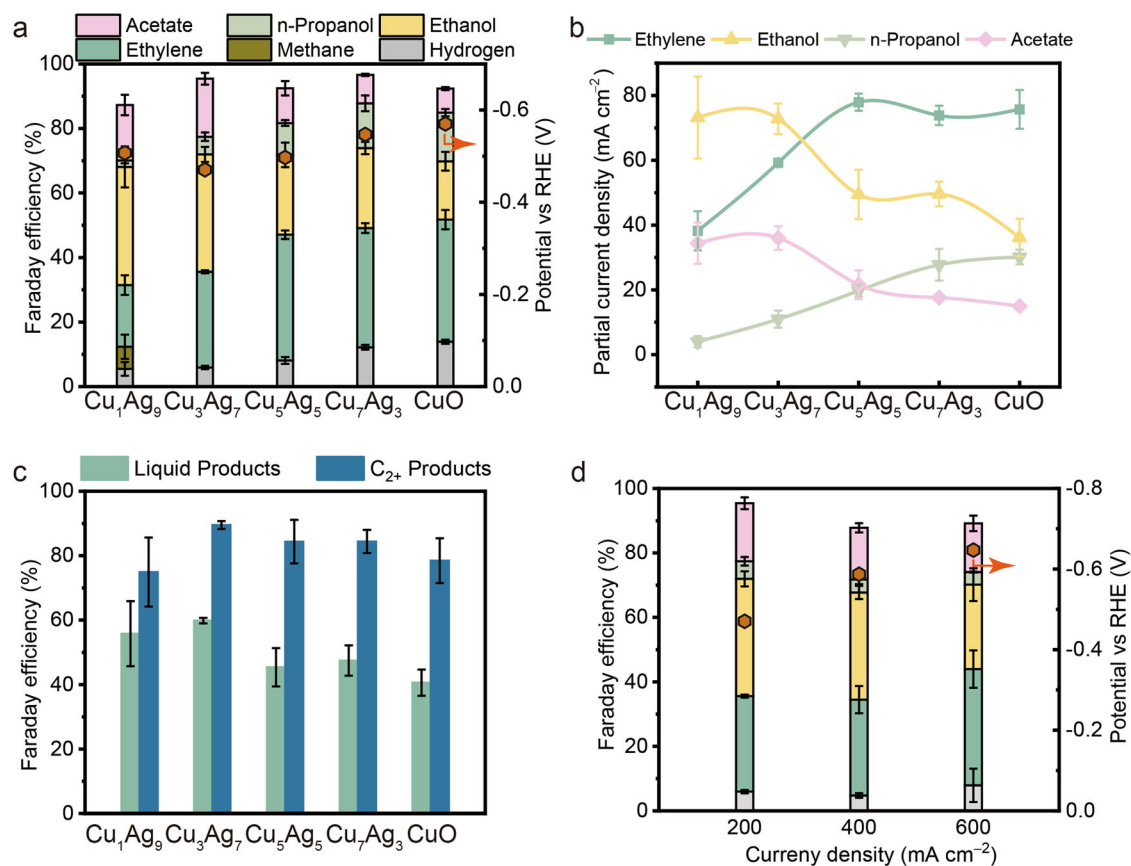


Fig. 4 | Electrochemical COR performance of CuO and the CuAg catalysts. a FEs of hydrogen, methane, ethylene, acetate, ethanol and propanol during COR at 200 mA cm⁻² on CuO and different CuAg catalysts. **b** Partial current densities of C₂₊ products for CuO and the CuAg catalysts with different Cu/Ag ratio at 200 mA cm⁻². **c** Total FEs of C₂₊ products and liquid products at 200 mA cm⁻² on CuO and CuAg

samples. **d** FEs of each product on Cu₃Ag₇ under different current densities and electrode potentials. The error bars represent standard deviations from at least three independent measurements. Relevant source data are provided as a Source Data file.

by below-average coordination numbers during COR. Therefore, we believe that this undercoordinated amorphous Cu prompts overall activity toward C₂₊ formation activity and meanwhile favors the production of liquid products^{79,80}. To validate our hypothesis, we conducted COR on a physical mixture of CuO and Ag₂O with the same atomic ratio as the CuAg catalysts. Under the same conditions, although the physically mixed Cu/Ag catalyst also exhibit reduced formation of H₂ with the increase of Ag content (Supplementary Fig. 18), the selectivity towards ethylene and liquid products resemble that of the pristine CuO catalyst. Hence, we can infer that the enhanced C₂₊ formation activity and improved liquid product selectivity is predominately resulted from the amorphous nature of the Cu. Note, our conclusion does not rule out the possibilities proposed by the recent studies on COR using other CuAg bimetallic materials, the variations are likely resulted from differences in the synthetic procedures employed for preparing the catalyst materials^{32,33,37,42}. For instance, the active sites suggested to be in close proximity to the Cu and Ag interface could also contribute to our scenario since the Cu and Ag are phase-separated¹⁴.

Previously, it was demonstrated that electrolysis involving the co-feeding of CO/CO₂ promotes the C₂₊ product formation during COR^{44,81,82}. Inspired by this, we explored whether this phenomenon could be extended in flow cells with higher current densities. Consequently, we carried out similar CO/CO₂ co-feeding electrolysis in flow cell at 200 mA cm⁻² (Fig. 5a, b). We also evaluated the electrocatalytic performance of the CuAg catalysts in pure CO₂ (CO₂R) for comparative analysis (Supplementary Fig. 19). Under the typical CO₂R condition, instead of C₂₊ products, CO emerges as the primary product,

particularly evident on catalysts with high Ag content such as Cu₃Ag₇. This result is anticipated since Ag is known as an active and selective catalyst for the CO₂ to CO conversion. Upon mixing CO with CO₂, depicted in Fig. 5a, b, both Cu₃Ag₇ and CuO exhibit enhanced formation rate for C₂₊ products. This phenomenon is more profound on Cu₃Ag₇, which is likely due to its improved activity for CO reduction as aforementioned. For instance, the primary product on Cu₃Ag₇ is CO with a rate of -9.67×10^{-7} moles s⁻¹ using pure CO₂ feeding at 200 mA cm⁻², and the production rate of C₂₊ is only 1.62×10^{-8} moles s⁻¹. Notably, upon introducing 25% CO into the feed stream, the production rate of C₂₊ products increase to 7.19×10^{-8} moles s⁻¹, which accounts for fivefold increase in comparison to pure CO₂R. However, this increasing trend in C₂₊ formation did not decline similarly to the previous studies^{44,81} when using only CO as the feed, on both Cu₃Ag₇ and CuO. At first glance, this phenomenon suggests that CO₂R may compete with COR for active sites, and COR pathways are inherently more active for C₂₊ production, within vapor fed devices. This result aligns well with a recent report, which highlighted the significance of conducting electrolysis under high CO concentrations⁸³. To validate this hypothesis, we firstly conduct identical co-feeding electrolysis using isotopically labeled ¹²CO/¹³CO₂ stream in 1M KOH. Surprisingly, as shown in Fig. 5c, all measurable C₂₊ products are originated from the ¹²CO on both Cu₃Ag₇ and CuO, indicating that they are derived from the COR pathway exclusively. Similar, though not identical, observations were made in a recent work⁴⁴, where the majority of C₂₊ products also originated from the COR pathway. The authors attribute this behavior to the hypothesis of Cu having distinct reaction sites on polycrystalline Cu, favoring the conversion of CO₂ to

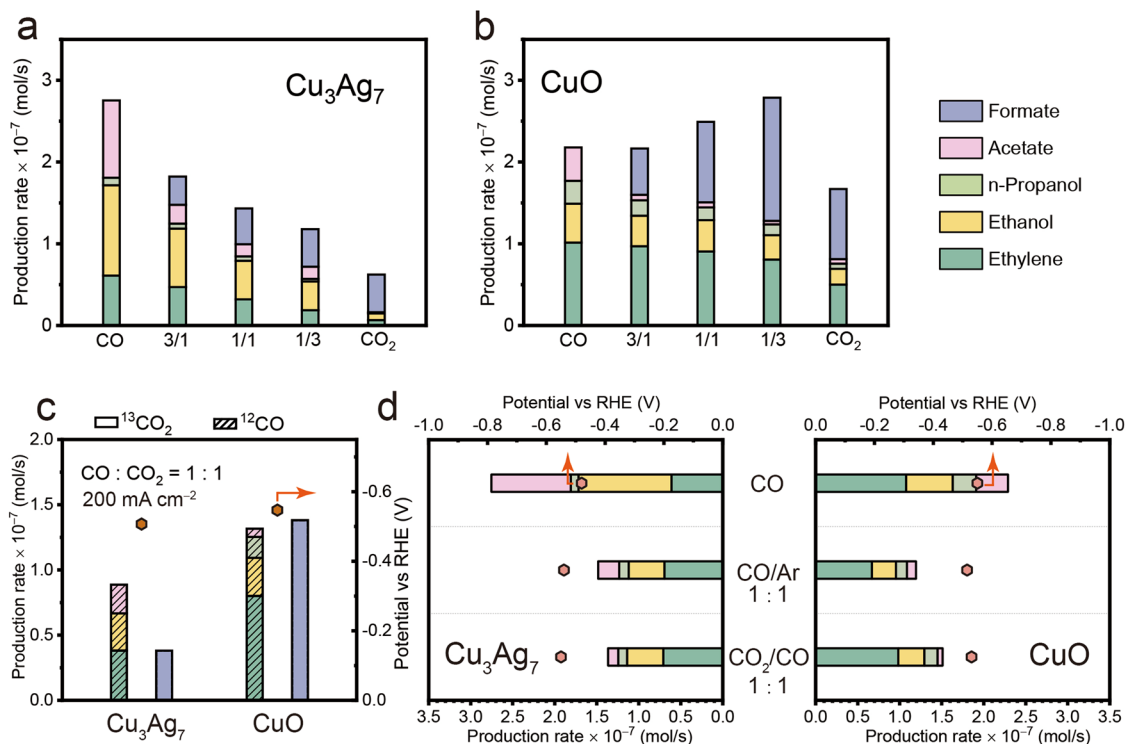


Fig. 5 | CO/CO₂ co-feeding electrolysis and isotopic labeling experiments. Production rates of hydrogen, carbon monoxide, ethylene, acetate, ethanol and propanol on **a** Cu₃Ag₇ and **b** CuO catalysts across various feed-gas ratios under 200 mA cm⁻². **c** Product distribution on Cu₃Ag₇ and CuO catalysts using isotopic

labeled stream of ¹³CO₂/¹²CO under 200 mA cm⁻². **d** C₂₊ products distribution on CuO and Cu₃Ag₇ catalysts across various feed-gas ratios. Relevant source data are provided as a Source Data file.

CO (Cu_{CO}) and the reduction of CO to C₂₊ (Cu_{CO}) products, respectively. We believe that in our case, the flow cell configuration provides a higher concentration of CO, which is expected to bind to the surface more readily, thereby saturating the Cu-active sites for C₂₊ production. Nevertheless, to provide additional evidence that CO₂ does not contribute to the formation of C₂₊ products under our testing conditions, we carried out Argon (Ar)/CO co-feeding electrolysis (Fig. 5d). Under similar applied overpotentials, the production rate of C₂₊ products on both Cu₃Ag₇ and CuO with Ar/CO feeding and CO₂/CO feeding is comparable, indicating that CO predominately contributes to the generation of C₂₊ products.

However, it is anticipated that not all CO₂ molecules participate in the electrochemical reaction due to the reaction between CO₂ and KOH. To investigate this effect further, we conducted identical CO/CO₂ co-feeding electrolysis using isotopically labeled ¹³CO₂ in electrolytes with varying pH, such as KHCO₃ and H₂SO₄. As shown in Supplementary Fig. 21b, c, upon mixing ¹²CO with ¹³CO₂, Cu₃Ag₇ demonstrates an enhanced formation rate for C₂₊ products in both 1 M KHCO₃ and 0.1 M H₂SO₄. The increasing trend of C₂₊ products remains consistent across different electrolytes when the CO content is increased, pinpointing the contribution of CO to the generation of C₂₊ products, as discussed previously. Note, despite the overall similar trends in product distributions, there are minor differences exists among different experiments, likely attributable to slight variations in the applied potentials in different systems. In all experiments, C₂₊ products are predominantly formed solely by ¹²C-atoms originating from ¹²CO, with a minor contribution from ¹³CO₂ (Supplementary Fig. 21f). For instance, over 80% of the ethanol and acetate produced originated solely from ¹²CO. Even in the remaining ~20% of the ethanol and acetate, ¹³C contributes only one carbon, specifically the methyl group in both products. Additionally, there are no C₂₊ products formed solely by ¹³C-atoms from ¹³CO₂. Therefore, we believe that ethanol and acetate are formed through the pathway of ¹²CO–¹³COH asymmetric

coupling⁸⁴. Nevertheless, these results further support our previous conclusion that the majority of C₂₊ products originated from the COR pathway under our testing conditions. It is important to note that an increase in local pH is inevitable even though acidic electrolytes are employed, therefore, we do not exclude the contribution of the reaction between a portion of CO₂ and KOH, thereby diminishing the contribution of CO₂ to C₂₊.

We also analyzed the production rate of formate during the co-feeding electrolysis. Notably, as shown in Fig. 5b, we observed an increase in formate production rate when blending the CO₂ stream with 25% CO, instead of decline. Since formate is expected to be formed exclusively from CO₂, we suppose that it is generated on the same type of active site as CO formation (Cu_{CO}), and the external CO feeding shifts the chemical equilibrium towards formation production. Nonetheless, as we further increase the CO concentration in the feed, the insufficient CO₂ partial pressure eventually leads to the decline in formate production (Fig. 5b). On the other hand, Cu₃Ag₇ exhibits substantially reduced production rate for formate, which is also relatively insensitive to the CO₂ partial pressure. We attribute this to the undercoordinated nature of the amorphous Cu layer on Cu₃Ag₇, which is consistent with the hypothesis proposed in previous work. It is likely that the Cu_{CO} sites associated with the close-packed facets, such as Cu (111). Nevertheless, as shown in Fig. 5a, b, we can conclude that the rates of CO₂ to formate conversion are comparable, if not higher, than those of C₂₊ formation. The introduction of Ag effectively suppresses the competing pathway for producing multi-carbon products.

Theoretical investigations for COR on amorphous Cu

Density functional theory (DFT) based calculations were conducted to understand the improved selectivity towards liquid oxygenates such as ethanol on amorphous Cu. An amorphous Cu structure (a-Cu) was constructed using ab initio molecular dynamics (AIMD) simulations, where the details can be found in the Method section and

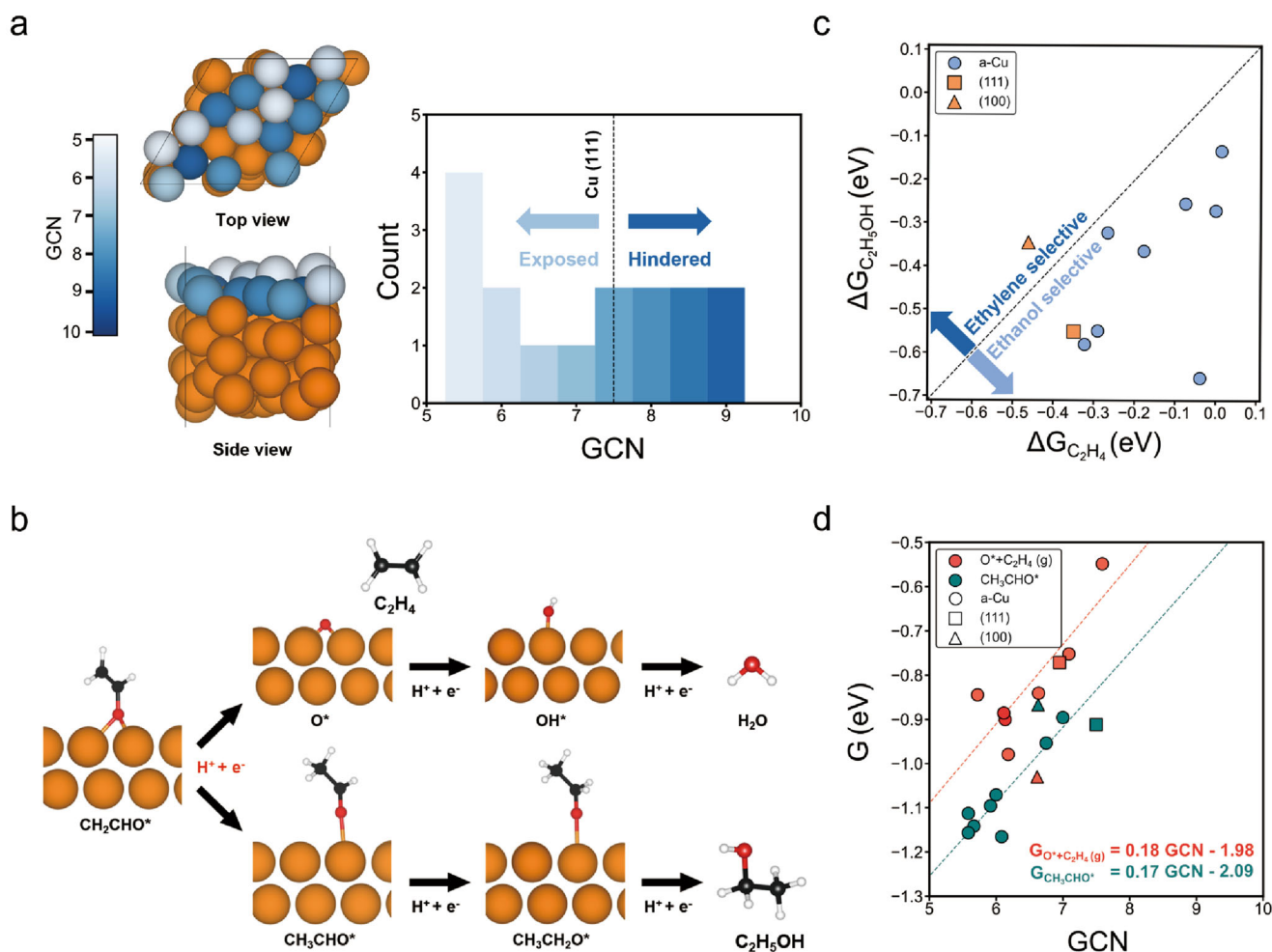


Fig. 6 | DFT calculations on Cu and amorphous Cu. a Top and side views of amorphous Cu (denoted as a-Cu), where darker colors indicate higher generalized coordination number (GCN) values. The histogram displays GCN in the exposed and hindered sites of the first layer. The dash line indicates the GCN calculated for an ideal Cu (111) surface. **b** Reaction pathway for ethylene and ethanol production by COR. The orange, red, black and white spheres represent the Cu, O, C, and H

atoms, respectively. **c** The Gibbs free energy changes of ethylene-selective pathway ($\Delta G_{C_2H_4}$) and ethanol-selective pathway ($\Delta G_{C_2H_5OH}$) on a-Cu illustrating the selectivity between two products. **d** The binding free energies of CH_3CHO^* (green) and $O^* + C_2H_4(g)$ (red) vs. GCN values of the active sites of a-Cu. The dashed line in panel d represents the observed correlation between the GCN of active sites and the binding free energies. Relevant source data are provided as a Source Data file.

Supplementary note 1. As shown in Fig. 6a, the a-Cu structure displays a roughened surface layer compared to the crystalline Cu (111) facet. For the outermost Cu atoms on the a-Cu surface layer, we characterized these sites with the generalized coordination number (GCN), an effective geometry descriptor that reflects the coordination environments of the Cu atoms (Supplementary Note 2 and Fig. 6a). Clearly, the Cu atoms exposed on the surface exhibit lower GCN values in comparison to the more hindered sites, all of which are lower than 7.5, the GCN value of an ideal Cu (111) surface atom. This result is in accordance with our EXAFS spectra, implying the reduction of the coordination number of the Cu (Fig. 3d). Considering the correlation between GCN values and binding energies, we anticipate that the a-Cu structure can enhance the reactivity of the surface Cu atoms (Supplementary Fig. 23)⁷⁹.

Previously, it has been proposed that the product selectivity between ethylene and ethanol depends on the energetics of reaction pathways involving the intermediate of CH_2CHO^* (Fig. 6b)^{84,85}. Specifically, ethylene is produced when the C atom in the CHO moiety within CH_2CHO^* is protonated, leading to the breaking of the C–O bond ($CH_2CHO^* \rightarrow O^* + C_2H_4(g)$). On the other hand, the production of ethanol occurs when C atom in the CH_2 within CH_2CHO^* undergoes protonation, followed by the consequent electron coupled

protonation steps ($CH_2CHO^* \rightarrow CH_3CHO^* \rightarrow C_2H_5OH(g)$). Thus, we calculated the Gibbs free energy changes of pathways leading to ethylene and ethanol, denoted as $\Delta G_{C_2H_4}$ and $\Delta G_{C_2H_5OH}$, respectively, and compared them across various adsorption sites on the a-Cu surface. Specifically, we calculated $\Delta G_{C_2H_4}$ and $\Delta G_{C_2H_5OH}$ as follows:

$$\Delta G_{C_2H_4} = G_{O^* + C_2H_4(g)} - G_{CH_2CHO^*} \quad (1)$$

$$\Delta G_{C_2H_5OH} = G_{CH_3CHO^*} - G_{CH_2CHO^*} \quad (2)$$

For all distinct exposed and hindered sites, we calculated and compared $\Delta G_{C_2H_4}$ and $\Delta G_{C_2H_5OH}$, where more energetically favorable $\Delta G_{C_2H_4}$ ($\Delta G_{C_2H_5OH}$) corresponds to selective production of ethylene (ethanol). We found that geometric relaxations of many hindered sites resulted in the relocation of adsorbates to the exposed sites, suggesting that the exposed sites are the predominate active sites on a-Cu. Therefore, only the exposed sites were considered for further calculations. As shown in Fig. 6c, we observed that all adsorption sites of a-Cu exhibited a more favorable $\Delta G_{C_2H_5OH}$, suggesting a general preference for ethanol formation over ethylene.

To gain deeper understandings of the enhanced ethanol selectivity on the a-Cu, we investigated the energetics of O* and CH₃CHO* in detail, as their binding strengths play critical roles in determining the selectivity^{86,87}. As shown in Fig. 6d, we observed strong correlations between the GCN of the active sites and the binding free energies of both O* and CH₃CHO*. Notably, while their slopes were found to be similar, $G_{\text{CH}_3\text{CHO}^*}$ exhibited lower y-intercept than $G_{\text{O}^*+\text{C}_2\text{H}_4(\text{g})}$. This implies that the ethanol pathway is generally more favorable than the ethylene pathway on active sites with the same GCN, with the exception of the Cu(100) sites. Furthermore, for a-Cu, O* adsorption mostly exhibits a higher GCN compared to CH₃CHO* adsorption due to O* preferring many-fold sites such as bridge or hollow sites, while CH₃CHO* prefers low-fold sites such as top or bridge sites. We also note that the GCN changes by less than 1 for various adsorption sites on crystalline Cu (111) and (100) facets (Supplementary Table 7), while it changes by more than 4 for a-Cu. This drastic difference results in a more significant stabilization of CH₃CHO* on a-Cu, consequently, leading to the selective production of ethanol. Overall, the computational simulations confirm that the improved selectivity and activity towards ethanol production on a-Cu originate from the amorphization of Cu, which reduces the coordination of surface atoms by roughening the surface.

Discussion

In this work, we interrogated the structural evolution of a typical Cu/Ag oxide-derived bimetallic catalyst during COR under practical relevant testing conditions. Through comprehensive in situ and ex situ characterizations, we found that the homogenous Cu/Ag oxide precursors undergo a structural transformation, resulting in a bimetallic composite comprising small Ag nanoparticles enveloped by thin and amorphous Cu layers. These amorphous Cu layers exhibit substantially reduced average coordination numbers compared to the polycrystalline Cu. As a result, this bimetallic catalyst demonstrates improved activity and high selectivity towards C₂₊ products (>90%), particularly liquid products (>60%), at high current densities under typical COR testing conditions. During CO₂/CO co-feeding electrolysis in the flow cell configuration, we found that a high CO concentration is more favorable for targeting C₂₊ product production. In addition, introducing Ag to Cu can suppress the competing pathway for formate production in the presence of CO₂. Furthermore, our DFT-based calculations further confirmed the low coordination nature of the amorphous Cu sites, and explained their high selectivity towards liquid products like ethanol, which is due to the favorable protonation of the C atom in the CH₂ moiety within the intermediate of CH₂CHO*. Overall, we believe our research can guide investigations into catalyst dynamic structural evolutions during electrochemical CO₂/CO reduction, offering insights for future catalyst and catalytic system design.

Methods

Chemicals and materials

Copper (II) nitrate trihydrate (Cu (NO₃)₂ · 3H₂O, 99.7%, trace metals basis), Silver nitrate (AgNO₃, ACS reagent, ≥99%), Sodium hydroxide (NaOH, reagent grade, ≥97%), Ethyl alcohol (C₂H₅O, ≥99%) were used as purchased from Sigma Aldrich. Potassium Hydroxide (KOH, 99.99%) was used as purchased from Macklin. Polytetrafluoroethylene (PTFE, 60 wt % dispersion in H₂O), Nafion™ perfluorinated resin solution (5 wt. % in mixture of lower aliphatic alcohols and water, contains 45% water) were used as purchased from Sigma Aldrich. The carbon paper (YLS-30T) was purchased from Su Zhou Sinero Technology Co., LTD. Anion exchange membrane (AEM, Selemion AMN/N type 1, AGC Inc.) was used to separate working and counter electrodes. CO and CO₂ were purchased from Air liquid. All chemicals are commercially available without further treatment. Ultra-pure water (18.2 MΩ · Cm, Millipore) was used throughout the experiments.

Synthesis of CuAg, CuO, and Ag₂O precursors

The CuAg precursors were synthesized as follows. First, Cu (NO₃)₂ and AgNO₃ with designed atomic ratio were dissolved in 10 mL H₂O. In total, 20 mL of sodium hydroxide solution containing 2.4 g NaOH was added into above solution and the brown precipitate formed instantly. After stirring for 1 h, the precipitate was transferred into 50-mL centrifuge tube and was centrifuged at 4830 × g for 5 min. The product was washed with water. After repeating this process for five times, the product was dried at 100 °C in air for 12 h. The CuO and Ag₂O precursors were prepared by the same process with Cu (NO₃)₂ and AgNO₃, respectively.

Material characterizations

The surface morphology of samples was characterized by JEOL JSM-7610F SEM. Transmission electron microscopy (TEM) image and X-ray energy-dispersive spectroscopy (XEDS) were obtained by a JEOL JEM-2010F TEM. X-ray diffraction (XRD, Bruker D8-advance) was applied to characterize the crystal structure with a Cu K-α as X-ray source ($\lambda = 1.5406 \text{ \AA}$). X-ray photoelectron spectroscopy (XPS) was conducted to analysis the surface chemical compositions on Kratos Axis Ultra spectrometer (Mono Al Kα, $h\nu = 1486.71 \text{ eV}$). High-angle annular dark-field scanning transmission electron microscopy (HAADF-STEM) and energy-dispersive X-ray spectroscopy were conducted on a JEOL ARM 200CF equipped with an Oxford Instruments X-ray energy-dispersive spectrometer.

Operando measurements

Operando X-ray absorption fine structure (XAFS) spectroscopy was performed at the XAFCA beamline of the Singapore Synchrotron Light Source in the fluorescence mode. A customized flow cell with alkaline (1 M KOH) electrolyte for COR was used. A Kapton tape was used to seal the gas chamber at the cathode side to allow the penetration of X-ray and fluorescence signals. Cu K-edge XAFS spectra were measured with electron energy of 0.7 GeV. X-ray absorption near-edge spectra (XANES) and extended X-ray absorption fine structure (EXAFS) spectra were analyzed by using Athena and Artemis included in the Demeter package. The standard reference material of Cu foil was measured in parallel. The energy was calibrated with Cu foil for Cu K-edge. Electrochemical tests were conducted with a CHI760E potentiostat. Cu K-edge XANES and EXAFS spectra were collected. All characterization were conducted at room temperature (−25 °C) and ambient pressure.

Preparation of gas diffusion electrode

The catalyst was sprayed on the carbon paper with $1 \times 1 \text{ cm}^{-2}$. In all, 1 mg CuO/CuAg precursors powder was dispersed in the mixed solution with 5 wt% Nafion solution and 1 ml of ethanol. The ratio between Nafion and catalysts powder is 4 μl Nafion/1 mg catalyst powder. The ink was dispersed in an ultrasonic machine for more than 5 min before being sprayed on the carbon paper. After the ink is prepared, the carbon paper is fixed on the heating plate. The ink was added into the spray gun to spray on the carbon paper with 1 mg/cm^2 to form catalyst film. Flow cell measurements were conducted in a self-made cell (1 cm² active area). This cell was assembled from the sequential stacking of a gas chamber, a catalyst-loaded gas diffusion electrode (GDE) cathode, a catholyte chamber (where an Ag/AgCl reference electrode locates), an anion exchange membrane, an anolyte chamber and an IrO₂-loaded Ti plate anode. The Ag/AgCl reference electrode was purchased from Gaoss Union (Model 1038) and used after calibration using a home-made standard hydrogen electrode. The IrO₂/Ti anode was prepared by etching the Ti mesh with boiling 6 M HCl (ACS reagent, 37%, Sigma Aldrich) for 40 min. Then the solution with 2 mL HCl, 18 mL isopropanol and 60 mg Iridium chloride hydrate (99.9%, Sigma Aldrich) was dip-coated on Ti mesh, followed by drying under 100 °C for 10 min and calcined in air at 500 °C for 10 min. The procedure was repeated

ten times. During the typical COR measurements, 22 sccm of CO was continuously fed to the gas chamber. The catholyte electrolyte (1 M KOH) was pumped to circulate through the catholyte chambers and anolyte chambers (1 M KOH) at the rate of 15 mL/min by a double-channel peristaltic pump. The pH of the electrolyte was measured using a benchtop pH Meter (Fisher Scientific AE150 Accumet).

Feed gases controlling

The flow rate is kept at 22 sccm constantly. With the increased amount of CO co-feeding, the feed-gas ratio is tuned from 3:1 (CO₂ to CO), 1:1 to 1:3. Accordingly, the concentration of CO₂ or CO in solution was dependent on the partial pressure of the gases in the atmosphere (298 K, 101.3 KPa).

Electrochemical measurements

A BioLogic VMP3 multichannel potentiostat/galvanostat with a built-in EIS analyzer was used for all the electrochemical measurements under ambient conditions (room temperature around 25 °C) and ambient pressure. The anion exchange membrane (Selemion AMN/N type 1, AGG Inc.) was used between the working and counter electrode compartments. CO was flowed through the working-electrode compartment, with the flow rate regulated by a mass flow controller at 22 sccm. All the electrochemical performances shown in this work were tested for 0.5 h. The potential readings were measured against Ag/AgCl and then converted to RHE with necessary iR compensation by equation:

$$E(\text{vs. RHE}) = E(\text{vs. Ag/AgCl}) + 0.197\text{V} + 0.0591\text{V} \times \text{pH} - iR \quad (3)$$

The solution resistances were tested using the impedance module in potentiostat (BioLogic VMP3) during each electrochemical measurement, and the corresponding solution pH was measured using a benchtop pH Meter (Fisher Scientific AE150 Accumet). The Faradic Efficiency (FE) of each product was calculated by following equation:

$$\text{FE}(\%) = \frac{\text{amount of the product (mol)} \times n \times F \left(\frac{\text{C}}{\text{mol}}\right)}{I(A) \times t(s)} \times 100 \quad (4)$$

where n represents the number of electrons transferred, F represents the Faradaic constant, and C represents the Coulomb number.

Product analysis

For each tested cathode potential, 1 ml of reactor exhaust gas was injected into a gas chromatograph (GC, Shimadzu 2014). Liquid products were measured by ¹H NMR spectrum (Bruker, 400 MHz system) with Phenol and DMSO as the internal standard. A 700 μL aliquot of post-reaction electrolyte was mixed with 35 μL of the internal standard (10 mM dimethyl sulfoxide and 50 mM phenol in D₂O solution) for quantification.

Computational details

Density functional theory (DFT) calculations were performed using Vienna Ab initio Simulation Package (version 5.4.4). The generalized gradient approximation with the revised Perdew-Burke-Ernzerhof (GGA-RPBE) functional was used to describe the exchange-correlation interactions. The cutoff energy was set to 500 eV, and the convergence tolerances of energy and force were set to 10^{−4} eV and 0.05 eV/Å, respectively. The Monkhorst-Pack k -point meshes were set to (2 × 2 × 1). A four-layered (4 × 4) supercell consisting of 64 atoms was used to model crystalline and amorphous Cu (111). Further details on the construction of amorphous Cu (a-Cu) can be found in the Supplementary note 1. The bottom two layers of the structures were fixed to their bulk positions during the relaxation. A vacuum layer of −15 Å along the z -direction was added.

We used the computational hydrogen electrode (CHE) method to include the effect of the applied potential. This method assumes an equivalent chemical potential for half the amount of H₂ gas and a proton-electron pair ($\mu(\text{H}^+ + \text{e}^-) = 0.5\mu(\text{H}_2)$) under standard conditions (pH = 0 and $P_{\text{H}_2} = 101,325$ Pa) in the absence of the applied potential ($U = 0$ V_{RHE}). The Gibbs free energies were calculated by adding the Gibbs free energy correction values (G_{corr}) to DFT energies (E_{DFT}), i.e., $G = E_{\text{DFT}} + G_{\text{corr}}$. The Gibbs free energy correction values of adsorbates (gaseous molecules) were calculated using the harmonic oscillator (ideal gas) approximation at 298.15 K as implemented in the Atomic Simulation Environment (ASE). We included the solvation effect using the implicit solvation method implemented as VaspSol. To correct DFT errors of gas-phase molecules originated from RPBE functional, we added +0.07 eV and +0.03 eV to the DFT energy of CO and C₂H₄ molecule, respectively.

The binding free energies of the reaction intermediates were calculated relative to gas-phase CO, H₂, and H₂O as follows:

$$G_{\text{CH}_3\text{CHO}^*} = E_{\text{CH}_3\text{CHO}^*} - E_* - 2E_{\text{CO}} - 2.5E_{\text{H}_2} + E_{\text{H}_2\text{O}} + G_{\text{corr}} \quad (5)$$

$$G_{\text{CH}_3\text{CHO}^*} = E_{\text{CH}_3\text{CHO}^*} - E_* - 2E_{\text{CO}} - 3E_{\text{H}_2} + E_{\text{H}_2\text{O}} + G_{\text{corr}} \quad (6)$$

$$G_{\text{O}^* + \text{C}_2\text{H}_4(\text{g})} = E_{\text{O}^*} - E_* - 2E_{\text{CO}} - 3E_{\text{H}_2} + E_{\text{H}_2\text{O}} + E_{\text{C}_2\text{H}_4} + G_{\text{corr}} \quad (7)$$

Data availability

Source data are provided with this paper and are available from the corresponding authors upon request.

References

- Jhong, H.-R. M., Ma, S. & Kenis, P. J. A. Electrochemical conversion of CO₂ to useful chemicals: current status, remaining challenges, and future opportunities. *Curr. Opin. Chem. Eng.* **2**, 191–199 (2013).
- Chu, S., Cui, Y. & Liu, N. The path towards sustainable energy. *Nat. Mater.* **16**, 16–22 (2016).
- Yang, Z. et al. Electrochemical energy storage for green grid. *Chem. Rev.* **111**, 3577–3613 (2011).
- Ma, M. Insights into the carbon balance for CO₂ electroreduction on Cu using gas diffusion electrode reactor designs. *Energy Environ. Sci.* **13**, 977–985 (2020).
- Louidice, A. et al. Tailoring copper nanocrystals towards C2 products in electrochemical CO₂ reduction. *Angew. Chem. Int. Ed.* **55**, 5789–5792 (2016).
- Morales-Guio, C. G. et al. Improved CO₂ reduction activity towards C2+ alcohols on a tandem gold on copper electrocatalyst. *Nat. Catal.* **1**, 764–771 (2018).
- Wang, X. et al. Efficient electrically powered CO₂-to-ethanol via suppression of deoxygenation. *Nat. Energy* **5**, 478–486 (2020).
- Bui, J. C. et al. Engineering catalyst-electrolyte microenvironments to optimize the activity and selectivity for the electrochemical reduction of CO₂ on Cu and Ag. *Acc. Chem. Res.* **55**, 484–494 (2022).
- Zheng, Y. et al. Understanding the roadmap for electrochemical reduction of CO₂ to multi-carbon oxygenates and hydrocarbons on copper-based catalysts. *J. Am. Chem. Soc.* **141**, 7646–7659 (2019).
- Verdaguer-Casadevall, A. et al. Probing the active surface sites for CO reduction on oxide-derived copper electrocatalysts. *J. Am. Chem. Soc.* **137**, 9808–9811 (2015).
- Wang, L. et al. Electrochemical carbon monoxide reduction on polycrystalline copper: effects of potential, pressure, and pH on selectivity toward multicarbon and oxygenated products. *ACS Catal.* **8**, 7445–7454 (2018).

12. Luc, W. et al. Two-dimensional copper nanosheets for electrochemical reduction of carbon monoxide to acetate. *Nat. Catal.* **2**, 423–430 (2019).
13. Pang, Y. et al. Efficient electrocatalytic conversion of carbon monoxide to propanol using fragmented copper. *Nat. Catal.* **2**, 251–258 (2019).
14. Li, C. W. Electroreduction of carbon monoxide to liquid fuel on oxide-derived nanocrystalline copper. *Nature* **508**, 504–507 (2014).
15. Bertheussen, E. et al. Acetaldehyde as an intermediate in the electroreduction of carbon monoxide to ethanol on oxide-derived copper. *Angew. Chem. Int. Ed.* **55**, 1450–1454 (2016).
16. Wang, X. et al. Efficient upgrading of CO to C3 fuel using asymmetric C-C coupling active sites. *Nat. Commun.* **10**, 5186 (2019).
17. Zhuang, T.-T. et al. Copper nanocavities confine intermediates for efficient electrosynthesis of C3 alcohol fuels from carbon monoxide. *Nat. Catal.* **1**, 946–951 (2018).
18. Li, J. et al. Constraining CO coverage on copper promotes high-efficiency ethylene electroproduction. *Nat. Catal.* **2**, 1124–1131 (2019).
19. Rosen, J. et al. Electrodeposited Zn dendrites with enhanced CO selectivity for electrocatalytic CO₂ reduction. *ACS Catal.* **5**, 4586–4591 (2015).
20. Verma, S. The effect of electrolyte composition on the electroreduction of CO₂ to CO on Ag based gas diffusion electrodes. *Phys. Chem. Chem. Phys.* **18**, 7075–7084 (2016).
21. Ma, M., Trzesniewski, B. J., Xie, J. & Smith, W. A. Selective and efficient reduction of carbon dioxide to carbon monoxide on oxide-derived nanostructured silver electrocatalysts. *Angew. Chem. Int. Ed.* **55**, 9748–9752 (2016).
22. Jhong, H. M. et al. A nitrogen-doped carbon catalyst for electrochemical CO₂ conversion to CO with High selectivity and current density. *ChemSusChem* **10**, 1094–1099 (2017).
23. Verma, S. et al. Insights into the low overpotential electroreduction of CO₂ to CO on a supported gold catalyst in an alkaline flow electrolyzer. *ACS Energy Lett.* **3**, 193–198 (2017).
24. Yin, J. et al. The built-in electric field across FeN/Fe3N interface for efficient electrochemical reduction of CO₂ to CO. *Nat. Commun.* **14**, 1724 (2023).
25. Vijay, S. et al. Unified mechanistic understanding of CO₂ reduction to CO on transition metal and single atom catalysts. *Nat. Catal.* **4**, 1024–1031 (2021).
26. Monteiro, M. C. O., Philips, M. F., Schouten, K. J. P. & Koper, M. T. M. Efficiency and selectivity of CO₂ reduction to CO on gold gas diffusion electrodes in acidic media. *Nat. Commun.* **12**, 4943 (2021).
27. Hori, Y. Electrochemical reduction of CO at a copper electrode. *J. Phys. Chem. B* **101**, 7075–7081 (1997).
28. Schouten, K. J. P. Two pathways for the formation of ethylene in CO reduction on single-crystal copper electrodes. *J. Am. Chem. Soc.* **134**, 9864–9867 (2012).
29. Guan, A. et al. Steric effect induces CO electroreduction to CH₄ on Cu–Au alloys. *J. Mater. Chem. A* **9**, 21779–21784 (2021).
30. Ji, Y. et al. Selective CO-to-acetate electroreduction via intermediate adsorption tuning on ordered Cu–Pd sites. *Nat. Catal.* **5**, 251–258 (2022).
31. Li, J. et al. Enhanced multi-carbon alcohol electroproduction from CO via modulated hydrogen adsorption. *Nat. Commun.* **11**, 3685 (2020).
32. Li, J. et al. Weak CO binding sites induced by Cu–Ag interfaces promote CO electroreduction to multi-carbon liquid products. *Nat. Commun.* **14**, 698 (2023).
33. Dorakhan, R. et al. A silver–copper oxide catalyst for acetate electrosynthesis from carbon monoxide. *Nat. Synth.* **2**, 448–457 (2023).
34. Martić, N. et al. Ag₂Cu₂O₃—a catalyst template material for selective electroreduction of CO to C₂+ products. *Energy Environ. Sci.* **13**, 2993–3006 (2020).
35. Chang, C. J. et al. Dynamic reoxidation/reduction-driven atomic interdiffusion for highly selective CO₂ reduction toward methane. *J. Am. Chem. Soc.* **142**, 12119–12132 (2020).
36. Wang, P. et al. Boosting electrocatalytic CO₂-to-ethanol production via asymmetric C-C coupling. *Nat. Commun.* **13**, 3754 (2022).
37. Qi, K. et al. Unlocking direct CO₂ electrolysis to C₃ products via electrolyte supersaturation. *Nat. Catal.* **6**, 319–331 (2023).
38. Clark, E. L., Hahn, C., Jaramillo, T. F. & Bell, A. T. Electrochemical CO₂ reduction over compressively strained CuAg surface alloys with enhanced multi-carbon oxygenate selectivity. *J. Am. Chem. Soc.* **139**, 15848–15857 (2017).
39. Ting, L. R. L. et al. Enhancing CO₂ electroreduction to ethanol on copper–silver composites by opening an alternative catalytic pathway. *ACS Catal.* **10**, 4059–4069 (2020).
40. Wang, L. et al. Selective reduction of CO to acetaldehyde with CuAg electrocatalysts. *Proc. Natl. Acad. Sci. USA* **117**, 12572–12575 (2020).
41. Cai, Z. et al. Hierarchical Ag–Cu interfaces promote C–C coupling in tandem CO₂ electroreduction. *Appl. Catal. B* **325**, 122310 (2023).
42. Chen, P. C. et al. Chemical and structural evolution of AgCu catalysts in electrochemical CO₂ reduction. *J. Am. Chem. Soc.* **145**, 10116–10125 (2023).
43. Subramanian, P. R. The Ag–Cu (silver–copper) system. *J. Phase Equilibria* **14**, 62–75 (1993).
44. Gao, W., Xu, Y., Fu, L., Chang, X. & Xu, B. Experimental evidence of distinct sites for CO₂-to-CO and CO conversion on Cu in the electrochemical CO₂ reduction reaction. *Nat. Catal.* **6**, 885–894 (2023).
45. Speck, F. D. & Cherevko, S. Electrochemical copper dissolution: a benchmark for stable CO₂ reduction on copper electrocatalysts. *Electrochem. Commun.* **115**, 106739 (2020).
46. Vavra, J., Shen, T. H., Stoian, D., Tileli, V. & Buonsanti, R. Real-time monitoring reveals dissolution/redeposition mechanism in copper nanocatalysts during the initial stages of the CO(2) reduction reaction. *Angew. Chem. Int. Ed.* **60**, 1347–1354 (2021).
47. Gómez-Romero, P. Ag₂Cu₂O₃: the first silver copper oxide. *Angew. Chem. Int. Ed.* **38**, 524–525 (1999).
48. Svintsitskiy, D. A. et al. Low-temperature catalytic CO oxidation over mixed silver–copper oxide Ag₂Cu₂O₃. *Appl. Catal. A-Gen.* **510**, 64–73 (2016).
49. Yin, C. et al. Synergistic activation of peroxymonosulfate for efficient aqueous p-nitrophenol degradation with Cu(II) and Ag(I) in Ag₂Cu₂O₃. *Sep. Purif. Technol.* **291**, 129034 (2022).
50. Kumar, R. V. Sonochemical synthesis of amorphous Cu and nanocrystalline Cu₂O embedded in a polyaniline matrix. *J. Mater. Chem.* **11**, 1209–1213 (2001).
51. Duan, Y. X. et al. Amorphizing of Cu nanoparticles toward highly efficient and robust electrocatalyst for CO₂ reduction to liquid fuels with high faradaic efficiencies. *Adv. Mater.* **30**, e1706194 (2018).
52. Wang, H. R. Crystallization processes in amorphous Zr₅₄Cu₄₆ alloy. *J. Non Cryst. Solids* **311**, 36–41 (2002).
53. Liu, X., Du, J., Shao, Y., Zhao, S. F. & Yao, K. F. One-pot preparation of nanoporous Ag–Cu@Ag core-shell alloy with enhanced oxidative stability and robust antibacterial activity. *Sci. Rep.* **7**, 10249 (2017).
54. Whittingham, A. W. H. & Smith, R. D. L. Electrochemically induced phase changes in La₂CuO₄ during cathodic electrocatalysis. *ChemElectroChem* **6**, 5116–5123 (2019).
55. Zhang, R. et al. Surface amorphization: a simple and effective strategy toward boosting the electrocatalytic activity for alkaline water oxidation. *ACS Sustain. Chem. Eng.* **5**, 8518–8522 (2017).
56. Liang, Y., Zhou, W., Shi, Y., Liu, C. & Zhang, B. Unveiling in situ evolved In/In₂O_{3-x} heterostructure as the active phase of In₂O₃

- toward efficient electroreduction of CO₂ to formate. *Sci. Bull.* **65**, 1547–1554 (2020).
57. Wang, J. et al. Redirecting dynamic surface restructuring of a layered transition metal oxide catalyst for superior water oxidation. *Nat. Catal.* **4**, 212–222 (2021).
 58. Liu, J. et al. The flexibility of an amorphous cobalt hydroxide nanomaterial promotes the electrocatalysis of oxygen evolution reaction. *Small* **14**, e1703514 (2018).
 59. Zhao, Y. et al. Surface reconstruction of ultrathin palladium nanosheets during electrocatalytic CO₂ reduction. *Angew. Chem. Int. Ed.* **59**, 21493–21498 (2020).
 60. Liu, J. & Guo, L. In situ self-reconstruction inducing amorphous species: a key to electrocatalysis. *Matter* **4**, 2850–2873 (2021).
 61. Su, X. et al. Operando spectroscopic identification of active sites in NiFe Prussian blue analogues as electrocatalysts: activation of oxygen atoms for oxygen evolution reaction. *J. Am. Chem. Soc.* **140**, 11286–11292 (2018).
 62. Gonzalez-Flores, D. et al. Heterogeneous water oxidation: surface activity versus amorphization activation in cobalt phosphate catalysts. *Angew. Chem. Int. Ed.* **54**, 2472–2476 (2015).
 63. Huang, J., Mensi, M., Oveisi, E., Mantella, V. & Buonsanti, R. Structural sensitivities in bimetallic catalysts for electrochemical CO₂ reduction revealed by Ag-Cu nanodimers. *J. Am. Chem. Soc.* **141**, 2490–2499 (2019).
 64. Xu, Y. et al. Tuning the selectivity of liquid products of CO₂RR by Cu-Ag alloying. *ACS Appl. Mater. Inter.* **14**, 11567–11574 (2022).
 65. Qiao, Y. et al. Mechanistic insights into aldehyde production from electrochemical CO₂ reduction on CuAg alloy via operando X-ray measurements. *ACS Catal.* **13**, 9379–9391 (2023).
 66. Yu, Y. et al. Bulk-immiscible CuAg alloy nanorods prepared by phase transition from oxides for electrochemical CO₂ reduction. *Chem. Commun.* **58**, 11163–11166 (2022).
 67. Gaur, A. Copper K-edge XANES of Cu(I) and Cu(II) oxide mixtures. *J. Phys. Conf. Ser.* **190**, 012084 (2009).
 68. Silversmit, G. et al. In-situ XAS study on the Cu and Ce local structural changes in a CuO-CeO₂/Al₂O₃ catalyst under propane reduction and re-oxidation. *J. Phys. Chem. Solids* **70**, 1274–1284 (2009).
 69. Queffelec, C. Investigation of copper oxidation states in plasmonic nanomaterials by XAS and Raman spectroscopy. *Phys. Chem. Chem. Phys.* **22**, 2199 (2020).
 70. Birhanu, M. K. et al. Copper and copper-based bimetallic catalysts for carbon dioxide electroreduction. *Adv. Mater. Interfaces* **5**, 1800919 (2018).
 71. Chandarak, S. Synchrotron X-ray absorption study of Cu and Mn doped BiFeO₃-BaTiO₃ multiferroic ceramics. *Ferroelectrics* **422**, 23–29 (2011).
 72. Xu, Y. et al. Low coordination number copper catalysts for electrochemical CO₂ methanation in a membrane electrode assembly. *Nat. Commun.* **12**, 2932 (2021).
 73. Li, R. et al. Short-range order in amorphous nickel oxide nanosheets enables selective and efficient electrochemical hydrogen peroxide production. *Cell Rep. Phys. Sci.* **3**, 100788 (2022).
 74. Qiao, L., Zizak, I., Zaslansky, P. & Ma, Y. The crystallization process of vaterite microdisc mesocrystals via proto-vaterite amorphous calcium carbonate characterized by cryo-X-ray absorption spectroscopy. *Crystals* **10**, 750 (2020).
 75. Timoshenko, J. et al. Steering the structure and selectivity of CO₂ electroreduction catalysts by potential pulses. *Nat. Catal.* **5**, 259–267 (2022).
 76. Grosse, P. et al. Dynamic changes in the structure, chemical state and catalytic selectivity of Cu nanocubes during CO₂ electroreduction: size and support effects. *Angew. Chem. Int. Ed.* **57**, 6192–6197 (2018).
 77. Vavra, J., Shen, T. H., Stoian, D., Tileli, V. & Buonsanti, R. Real-time monitoring reveals dissolution/redeposition mechanism in copper nanocatalysts during the initial stages of the CO₂ reduction reaction. *Angew. Chem. Int. Ed.* **60**, 1347–1354 (2021).
 78. da Silva, A. H. M., Lenne, Q., Vos, R. E. & Koper, M. T. M. Competition of CO and acetaldehyde adsorption and reduction on copper electrodes and its impact on n-propanol formation. *ACS Catal.* **13**, 4339–4347 (2023).
 79. Chen, C. et al. Oxidation of metallic Cu by supercritical CO₂ and control synthesis of amorphous nano-metal catalysts for CO₂ electroreduction. *Nat. Commun.* **14**, 1092 (2023).
 80. Hu, F. et al. Ultrastable Cu catalyst for CO₂ electroreduction to multicarbon liquid fuels by tuning C-C coupling with CuTi subsurface. *Angew. Chem. Int. Ed.* **60**, 26122–26127 (2021).
 81. Wang, X. et al. Mechanistic reaction pathways of enhanced ethylene yields during electroreduction of CO₂-CO co-feeds on Cu and Cu-tandem electrocatalysts. *Nat. Nanotechnol.* **14**, 1063–1070 (2019).
 82. Möller, T., Filippi, M., Brückner, S., Ju, W. & Strasser, P. A CO₂ electrolyzer tandem cell system for CO₂-CO co-feed valorization in a Ni-N-C/Cu-catalyzed reaction cascade. *Nat. Commun.* **14**, 5680 (2023).
 83. Wei, P. et al. Coverage-driven selectivity switch from ethylene to acetate in high-rate CO₂/CO electrolysis. *Nat. Nanotechnol.* **18**, 299–306 (2023).
 84. Hanselman, S., Koper, M. T. M. & Calle-Vallejo, F. Computational comparison of late transition metal (100) surfaces for the electrocatalytic reduction of CO to C₂ species. *ACS Energy Lett.* **3**, 1062–1067 (2018).
 85. Calle-Vallejo, F. & Koper, M. T. Theoretical considerations on the electroreduction of CO to C₂ species on Cu(100) electrodes. *Angew. Chem. Int. Ed.* **52**, 7282–7285 (2013).
 86. Piqué, O., Viñes, F., Illas, F. & Calle-Vallejo, F. Elucidating the structure of ethanol-producing active sites at oxide-derived Cu electrocatalysts. *ACS Catal.* **10**, 10488–10494 (2020).
 87. Cheng, D. et al. The nature of active sites for carbon dioxide electroreduction over oxide-derived copper catalysts. *Nat. Commun.* **12**, 395 (2021).

Acknowledgements

The authors acknowledge the National University of Singapore and the Ministry of Education for their financial support, through the grants A-0009176-02-00 and A-0009176-03-00, as well as A*STAR (Agency for Science, Technology and Research) under its LCERFI program (award no. U2102d2002). We would also like to acknowledge the support of the National Research Foundation (NRF) Singapore, under the NRF Fellowship (NRF-NRFF13-2021-0007), as well as the support from the Centre for Hydrogen Innovations at the NUS (CHI-P2022-06; A-8000138-03-00). S.B. acknowledges the support from the Nano & Material Technology Development Program through the National Research Foundation of Korea (NRF) funded by Ministry of Science and ICT (RS-2024-00406517) and the Carbon Neutral Industrial Strategic Technology Development Program (RS-2023-00261088) funded by the Ministry of Trade, Industry & Energy (MOTIE, Korea). Qian He would like to acknowledge the support of the National Research Foundation (NRF) Singapore under its NRF Fellowship (NRF-NRFF11-2019-0002).

Author contributions

L.W. and D.W. conceived and designed this project. H.D.J. conducted the computational calculation and relative data analysis under the supervision of S.B. D.W. and J.C. synthesized the catalysts. D.W. and H.Y. conducted the operando XAS experiments under the supervision of S.X. S.L. performed HAADF-STEM characterizations under the supervision of Q.H. D.W., H.D.J., S.X., S.B., and L.W. contributed to data analysis and edited the manuscript. L.W. supervised the entire project.

Competing interests

The authors declare no competing interests.

Additional information

Supplementary information The online version contains supplementary material available at <https://doi.org/10.1038/s41467-024-49158-4>.

Correspondence and requests for materials should be addressed to Qian He, Shibo Xi, Seoin Back or Lei Wang.

Peer review information *Nature Communications* thanks the anonymous reviewers for their contribution to the peer review of this work. A peer review file is available.

Reprints and permissions information is available at <http://www.nature.com/reprints>

Publisher's note Springer Nature remains neutral with regard to jurisdictional claims in published maps and institutional affiliations.

Open Access This article is licensed under a Creative Commons Attribution 4.0 International License, which permits use, sharing, adaptation, distribution and reproduction in any medium or format, as long as you give appropriate credit to the original author(s) and the source, provide a link to the Creative Commons licence, and indicate if changes were made. The images or other third party material in this article are included in the article's Creative Commons licence, unless indicated otherwise in a credit line to the material. If material is not included in the article's Creative Commons licence and your intended use is not permitted by statutory regulation or exceeds the permitted use, you will need to obtain permission directly from the copyright holder. To view a copy of this licence, visit <http://creativecommons.org/licenses/by/4.0/>.

© The Author(s) 2024